ACS APPLIED MATERIALS & INTERFACES

www.acsami.org

Research Article

Matrix-Insensitive Sensor Arrays via Peptide-Coated Nanoparticles: Rapid Saliva Screening for Pathogens in Oral and Respiratory Diseases

Benjamin Lam, Lubna Amer, Elizabeth Thompson, Alex E. Clark, Aaron F. Garretson, Aaron F. Carlin, Casey Chen, Maurice Retout,* and Jesse V. Jokerst*

Cite This: *ACS Appl. Mater. Interfaces* 2024, 16, 67362−67372

Read Online

ACCESS | Metrics & More | Article Recommendations | Supporting Information

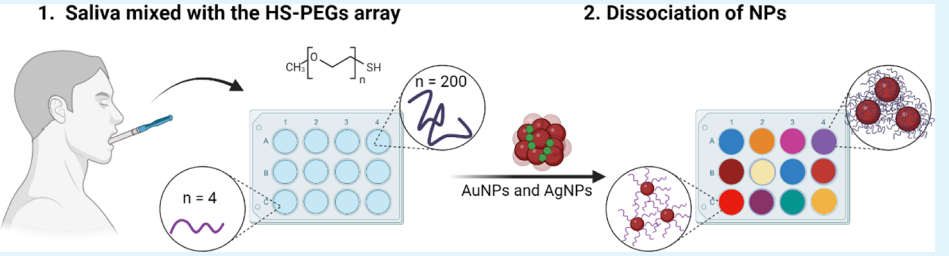

ABSTRACT: Plasmonic nanoparticle-based biosensors often report a colorimetric signal through the aggregation or clustering of the nanoparticles (NPs), but these mechanisms typically struggle to function in complex biofluids. Here, we report a matrix-insensitive sensor array approach to detect bacteria, fungi, and viruses whose signal is based on the dissociation of the peptide-aggregated NPs by thiolated polyethylene glycol (HS-PEG) polymers. We show that the HS-PEGs of differing sizes have varying capabilities to dissociate citrate-capped gold nanoparticle (AuNP) and silver nanoparticle (AgNP) assemblies. The dissociative abilities of the HS-PEGs were used in this sensor array to discriminate at the 90% confidence level the microorganisms *Porphyromonas gingivalis*, *Fusobacterium nucleatum*, and *Candida albicans* in water and saliva using linear discriminant analysis (LDA). We further demonstrate the versatility of the sensor array by detecting various subtypes of the viruses SARS-CoV-2 (beta, delta, and omicron) and influenza (H3N2) spiked in saliva samples using LDA. In the final demonstration, the sensor array design stratified healthy saliva samples from patient samples diagnosed with periodontitis as well as COVID-19.

KEYWORDS: *bacteria detection, colorimetric test, fungi detection, gold and silver nanoparticles, PEGs, reversible assembly, saliva, virus detection*

INTRODUCTION

Colorimetric biosensors provide visual cues that alert users of the presence or absence of a particular biomarker.[1] These point-of-care devices are particularly useful because the colorimetric signal allows patients to self-diagnose and can streamline the use of care facilities.[2,3] The use of plasmonic nanoparticles, particularly gold nanoparticles (AuNPs) and silver nanoparticles (AgNPs), provide a colorimetric signal based upon their localized surface plasmon resonance (LSPR) in the visible region.[4] These nanoparticles (NPs) exhibit shifts in their LSPR upon assembly, and the changes in color can detect diverse analytes, including proteases,[5] mRNA,[6] proteins,[7] and heavy metal ions.[8] However, the mechanism to induce the aggregation of the NPs often requires carefully engineered receptors to produce a specific interaction between the NPs and the target. For instance, the detection mechanism may use a specific amino acid cleavage sequence,[9] the complementarity of an antibody for an antigen,[10] the tailoring of an inhibitor for a catalyst,[11] or the targeting of a phage for a membrane receptor.[12]

In contrast, sensor arrays utilize nonspecific differences across an array of channels to discriminate different conditions. Many NP-based sensor array strategies depend on the aggregation or catalytic changes of the NPs in response to the analyte.[13] Through pattern recognition and statistical analysis of the channels, the responses can be separated through methods such as principal component analysis (PCA), linear discriminant analysis (LDA), and hierarchical clustering analysis (HCA).[14] Moreover, sensor arrays can also be utilized

Received: September 12, 2024
Revised: November 12, 2024
Accepted: November 15, 2024
Published: November 26, 2024

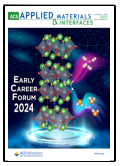

to detect multiple analytes rather than having a unique receptor for each target.

The application of plasmonic nanoparticles in sensor arrays toward sensing in biofluids, however, often faces challenges due to the compositional complexity of the media. The presence of salts, off-target proteins, and variations in pH may lead to false positives and false negatives.[15,16] The adsorption of proteins onto plasmonic nanoparticles can lead to protein coronas that may change the properties of the nanoparticle and affect their utility as colorimetric reporters.[17,18]

We recently developed a method to produce a colorimetric signal with AuNPs and AgNPs to detect the enzymatic activity of *Porphyromonas gingivalis* that is matrix-insensitive.[19] By dissociating the peptide-aggregated NPs with a thiolated polyethylene glycol (HS-PEG) polymer, a colorimetric response was capable of being produced in a broad range of physiological conditions, including saliva, plasma, urine, and even bile.[19] This mechanism, however, was only specific to *Porphyromonas gingivalis* because the sensor design was engineered to make it selective for the gingipain protease.[19]

Herein, we report a dissociation strategy for designing sensor arrays for the sensing of saliva infected with bacteria, fungi, or viruses. The AuNPs and the AgNPs are first aggregated by the peptide Arg-Arg-Lys (RRK). Importantly, this peptide-induced NP assembly is reversible, unlike salt-induced aggregation, because salt ions provide less steric hindrance than peptides; this steric bulk from the peptide is needed to prevent the aggregated NPs from falling into an irreversible energy minimum.[5] The peptide-driven nanoparticle assembly is then dissociated upon the addition of HS-PEGs, thus producing a change in the absorbance. We demonstrate that HS-PEGs of varying sizes have distinct capacities to dissociate the NP assemblies but also have distinct properties and, therefore, will interact with the target analyte differently. We also show that these differences in interaction can be discriminated with LDA at the 90% confidence level. We illustrate the use of this sensor array strategy to distinguish between clinical samples of patients with stage III periodontitis versus healthy patients as well as those infected with SARS-CoV-2.

EXPERIMENTAL SECTION

Citrate-Capped AuNPs. Citrate-stabilized AuNPs (~20 nm) were prepared using a previously reported procedure.[5] In short, this procedure utilized the Turkevich method for synthesizing AuNPs. Sodium citrate tribasic dihydrate (150 mg, 5 mL) was added to $HAuCl_4 \cdot 3H_2O$ (45 mg, 300 mL) under boiling conditions and vigorous stirring. After 15 min, the solution mixture was cooled to room temperature. The solution was then purified by centrifugation at 18,000*g* for 30 min, and then the supernatant was discarded. The AuNPs were redispersed in deionized water and stored at ambient conditions.

NPs Assembly. The NPs were assembled by mixing an aqueous solution of 100 μL NPs-citrate (AuNPs or AgNPs) at OD = 1 with 2 μL of RRK (500 μM) to induce the NPs assembly.[19] The solvent of the nanoparticles and the peptide was deionized water. The solution color with the assembled AgNPs changed from yellow to blue, while the solution color with the assembled AuNPs changed from red to blue. The assembled NPs were stable over time and were stored at 4 °C.

Evaluation of AgNP Stability. The drying and solubilization of the AgNPs were adapted from a previous procedure.[5] In short, the RRK-aggregated AgNPs were dried in a microcentrifuge tube overnight at 40 °C. The resulting dried assemblies were then stored for 10 days at 4 °C, 25 °C, and 37 °C to evaluate their stability at varying storage temperatures. Afterward, the dried assemblies were solubilized with deionized water, and the UV−vis spectra was measured using a hybrid multimode microplate reader (Synergy H1 model, BioTek Instruments, Inc.).

Sensor Array. Within a 96-well plate, 5 μL of the desired sample was mixed with 10 μL of the HS-PEG receptor. After 15 min, 100 μL of the assembled NPs (AgNPs or AuNPs) were added and 15 min later, the UV−vis signal was recorded using a hybrid multimode microplate reader (Synergy H1 model, BioTek Instruments, Inc.). The processing by LDA was done with R software as previously reported.[20]

Evaluation of pH Effects on HS-PEG Dissociation Ability. The pH of the RRK-aggregated nanoparticles (AuNPs or AgNPs) was adjusted using 0.1 M HCl to decrease the pH and 0.1 M NaOH to increase the pH. The final pH after addition of the HS-PEGs was measured and recorded using an Apera Instruments LabSen 241-3SP pH probe. The pH probe was calibrated with Apera Instruments buffer solutions at pH 4, 7, and 10 prior to use. The assembly intensity after pH modification and addition of the HS-PEGs was measured using a hybrid multimode microplate reader (Synergy H1 model, BioTek Instruments, Inc.).

Viral Isolation, Propagation, and Inactivation. SARS-CoV-2 strains (beta, delta, and omicron) were isolated, propagated, and UV-inactivated according to a previous procedure.[20] To summarize, the viruses were inoculated on TMPRSS2-VeroE6 cells, and the stocks were verified with whole-genome sequencing. The viral RNA concentrations were measured through droplet digital polymerase chain reaction (ddPCR). The viruses were then UV-inactivated and stored at −80 °C until use. Influenza A was propagated on MDCK cells, UV-irradiated, and verified as above. Inactivated viruses were serially diluted to the desired concentration with deionized water. Infectious SARS-CoV-2 was handled under BSL3 conditions in accordance with the UC San Diego Institutional Biosafety Committee, and inactivation was verified prior to removal to BSL2.

Fungal Culture. *C. albicans* was cultured according to a previous procedure.[21] In short, *C. albicans* was cultured on an agar plate from a lyophilized stock and incubated at 30 °C. A single colony of the fungus was then extracted and inoculated in a YEPD medium (2% Bactopeptone, 2% dextrose, 1% yeast extract in H_2O). The inoculated colony was allowed to grow overnight under gentle shaking at 30 °C. The resulting fungal culture was diluted 1:100, and the OD600 was measured to determine the cell concentration. An OD600 value of 0.5 corresponded to approximately 1×10^7 cells/mL.

Bacteria Culture. *P. gingivalis* and *F. nucleatum* were cultured according to a previous procedure.[21] To summarize, the bacteria were grown on agar plates from lyophilized stocks under anaerobic conditions at 37 °C. A single bacteria colony was then transferred to enriched tryptic soy broth (eTSB) and cultured overnight. Briefly, 500 mL of eTSB was prepared by dissolving 15 g tryptic soy broth, 2.5 g yeast extract, and 2.5 mL hemin (1 mg/mL) in 450 mL DI water; the pH of the eTSB was then adjusted to 7.4 using NaOH and DI water. The broth was then autoclaved, cooled to room temperature, and enriched with L-cysteine (5% w/v), 10 mL dithiothreitol (1% w/v), and 2 mL menadione (0.5 mg/mL).

GCF Collection. The gingival crevicular fluid (GCF) was collected according to a previous procedure.[19] In short, samples were collected using a curet and stored at −20 °C in 250 μL 20 mM Tris pH 7.4 + 5% glycerol. The study protocol received approval from the UCSD and USC Institutional Review Boards (HS-19-00163-CR002) and was in accordance with the ethical guidelines established by the Helsinki Declaration of 1975 for research with human subjects. Volunteer subjects provided informed consent and were selected from patients receiving dental treatment at the Herman Ostrow School of Dentistry. The patients were diagnosed with Stage III periodontitis according to the 2017 World Workshop on the Classification of Periodontal and Peri-implant Diseases and Conditions.

RESULTS AND DISCUSSION

We first explain how the sensor array was designed. The mechanism of this strategy is based upon preassembling

https://doi.org/10.1021/acsami.4c15662
ACS Appl. Mater. Interfaces 2024, 16, 67362−67372

Scheme 1. Description of the sensor array. The sensor array is composed of a library of various HS-PEGs of different sizes. The saliva sample is added to every well, and after 15 min, the RRK-aggregated NPs (gold or silver) are added as colorimetric reporters. The channels of the sensor array produce varying colorimetric responses based on the nonspecific interactions of the analytes in the sample with the HS-PEGs and the NPs

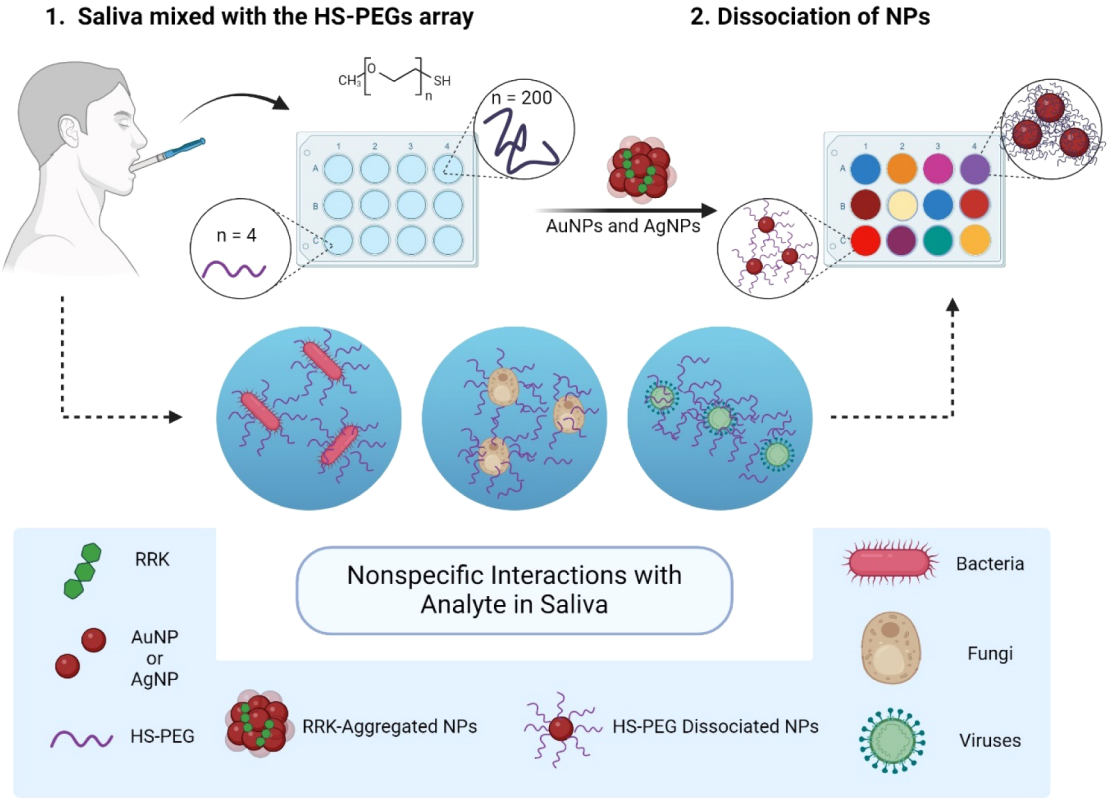

AuNPs and AgNPs with the RRK peptide and dissociating the NPs with HS-PEGs. We characterize this phenomenon by measuring the absorbance shifts of the NPs in response to aggregation and dissociation. The dissociative ability of the HS-PEGs used in the channels of the sensor array as a function of the polymer length is also examined. The sensor array is then used to detect microorganisms associated with periodontal disease in water and saliva using LDA. The optical responses from clinical saliva samples of patients with stage III periodontitis are also compared to those of healthy patients. The sensor array is then applied to discriminate variants of SARS-CoV-2 from the influenza virus as well as clinical samples with LDA. Finally, the limitations of this sensor array strategy are evaluated.

Sensor Array Design. Scheme 1 illustrates the sensor array strategy. The sensor array consists of a library of HS-PEGs of different sizes and one HS-PEG with a terminal carboxylic acid group instead of a methoxy group. The differences in size and end group would lead to variations in the chemical and physical properties of the HS-PEGs.[22,23] We reasoned that the varying size and hydrophilicity of the HS-PEGs would contribute to differences in the optical response of each channel and facilitate sensing of the target analyte because of differences in their nonspecific interaction. For instance, these nonspecific interactions between the analyte, the HS-PEGs, and the NPs may arise due to van der Waals forces, hydrogen bonding, hydrophobic interactions, and physical adsorption.[24]

Citrate-capped AuNPs and AgNPs were chosen as colorimetric reporters due to their LSPR in the visible region that allows for detection by eye.[25] A size of 20 nm was selected for both the AuNPs and the AgNPs in this sensor array because larger sized nanoparticles (>80 nm) produce less visible changes upon aggregation.[26,27] Larger sized nanoparticles have also been reported to be more colloidally stable which may hinder the dynamics of the sensor array design by requiring greater concentrations of materials to induce aggregation.[28] For instance, 50 nm AgNPs were reported to be more resistant to aggregation from salt and biomolecules than 10 and 20 nm AgNPs.[28] This enhanced stability and decreased surface reactivity may arise because larger nanoparticles have a lower surface area to volume ratio.[29] As a result, the 50 nm AgNPs have proportionally less unbound surface atoms and would be less energetically disfavored. Therefore, they would be less likely to aggregate. We have also previously shown that 80 nm AgNPs required greater amounts of peptide to induce aggregation compared to 25 nm AgNPs.[20] This may be due to greater electrostatic repulsion from more citrates coating the larger surface area, which would require more peptides to neutralize the charge. Larger nanoparticles may also be harder to dissociate with the HS-PEGs because of increased van der Waals forces between the nanoparticles.[30,31] Some studies have also suggested that smaller nanoparticles (<5 nm) are more toxic than larger nanoparticles.[32] Therefore, 20 nm nanoparticles may provide a better balance of colorimetric utility and safety for consumers and the environment compared to nanoparticles with more extreme sizes. However, optimization of the nanoparticle size for the sensor array was not explored in this study.

https://doi.org/10.1021/acsami.4c15662
ACS Appl. Mater. Interfaces 2024, 16, 67362−67372

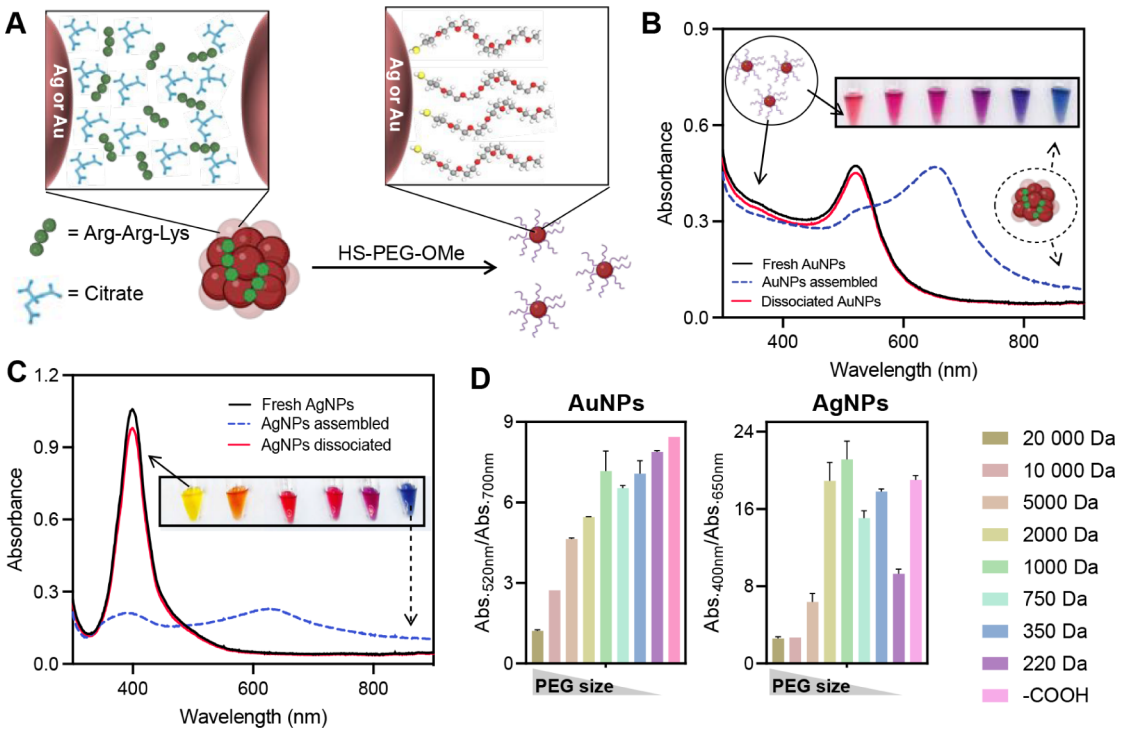

Figure 1. Dissociation of NPs assembly with HS-PEGs. (A) Scheme that illustrates the composition of the assembly and how the particles dissociate after grafting of the HS-PEGs onto the metallic surface. Panels (B) and (C) show the evolution of the optical properties of the assemblies upon dissociation with HS-PEGs. The absorbance values are measured in arbitrary units (a.u.). The inset images show the color range that can be obtained. Panel (D) summarizes the ratiometric absorbance values obtained for both AuNPs and AgNPs after addition of HS-PEGs of various sizes. The error bars represent the standard deviation from four replicates.

Figure 1A illustrates the disassembly of the peptide-assembled NPs. First, the positively charged peptide Arg-Arg-Lys (RRK) induces the aggregation of the negatively charged citrate-capped AuNPs and AgNPs.[5] This aggregation occurs through an electrostatic interaction between the peptide and the nanoparticles.[33] The positively charged guanidinium group would be attracted to the citrate ligand similar to the electrostatic interaction of guanidinium-carboxylate salt bridging.[34] The interaction of the peptide to the nanoparticle's negatively charged surface neutralizes the charge and reduces the electrostatic repulsion between citrate-capped nanoparticles. In turn, van der Waals forces can cause attraction; hence, the particles aggregate. Our prior work has shown that the addition of an uncharged peptide such as Gly-Gly (GG) does not induce aggregation of the nanoparticles even at concentrations exceeding 100 μM.[5,19,20]

The HS-PEG then dissociates the assembly due to the greater affinity of the thiol bond than the electrostatic attraction of the peptide for the metallic surface of the NPs.[19,33] The binding of the HS-PEG results in greater steric hindrance between the nanoparticles, resulting in their dissociation. The presence of the thiol anchoring group on the HS-PEG has been shown to be essential in the dissociation mechanism; when the anchoring group was replaced with a hydroxy group, the dissociative ability of the PEG was lost because the hydroxy group cannot strongly bind to the nanoparticle surface.[5] PEG polymers without a thiol could not dissociate the nanoparticles because there was not sufficient affinity of the polymer for the nanoparticle surface.[5] Figure 1B shows the shift in the absorbance spectra of the AuNPs before and after dissociation with the HS-PEGs. Initially, the RRK-aggregated AuNPs have an absorbance peak at around 700 nm, but upon dissociation, there is a hypsochromic shift back to near 520 nm. The inset photo highlights the color change of the AuNPs from blue to red upon dissociation. Similarly, Figure 1C compares the absorbance spectra of aggregated and dissociated AgNPs. The absorbance peak near a wavelength of 600 nm for the aggregated AgNPs is reverted to approximately 400 nm for the dissociated AgNPs. Unlike the AuNPs, there is a broader range of colors arising from the degree of dissociation. This is because the LSPR of AgNPs can be tuned over a broader range of wavelengths in the visible region compared to AuNPs.[35] TEM images were taken to confirm the aggregation and dissociation of the AuNPs and AgNPs (Figure S1). The images indicate that the clustering of the NPs was indeed reverted upon the addition of the HS-PEG.

A ratiometric absorbance value was used to quantify the aggregated and dissociated states of the NPs. The peak wavelengths of 520 and 700 nm were chosen for the AuNPs, while the peak wavelengths of 400 and 600 nm were chosen for the AgNPs. Thus, a high $Abs._{520\ nm}/Abs._{700\ nm}$ value would indicate greater dissociation for the AuNPs, and a high $Abs._{400\ nm}/Abs._{650\ nm}$ value would indicate greater dissociation for the AgNPs.

The capacity of the HS-PEGs to dissociate the NP assembly is dependent on the size of the polymer. The HS-PEG molecular weight examined ranged from 220 Da to 20 000 Da. This corresponds to lengths of approximately 0.7 to 11 nm based on the Flory radius.[36] Figure 1D provides the ratiometric absorbance values after dissociation as a function of the HS-PEGs used in the sensor array. These values show the dissociation pattern obtained in water in the absence of any target. Generally, the shorter HS-PEGs were more effective in dissociating the assembled NPs. This may be because longer

https://doi.org/10.1021/acsami.4c15662
ACS Appl. Mater. Interfaces 2024, 16, 67362−67372

HS-PEGs exhibit greater steric bulk that lessen their affinity for the surface of the NP.[19] The ratiometric absorbance values were then plotted as a function of the HS-PEG Flory radius (Figure S2). Based on the linear regression equations, the ratiometric absorbance value increases by 1.55 for the AgNPs and by 0.62 for the AuNPs per each nanometer decrease of the Flory radius. These slopes were significantly nonzero with *p*-values of 0.0006 and <0.0001 for the AgNPs and AuNPs, respectively. The greater magnitude in the slope for the AgNPs suggests greater sensitivity of the AgNPs to the size of the HS-PEG and may be due to the higher molar absorption coefficient of AgNPs compared to AuNPs.[37]

The sensor array design takes advantage of the differences in dissociation capability of the HS-PEGs by placing them in different channels. The target analyte of the sensor array would also interact differently with each HS-PEG and the NPs due to the unique physical and chemical properties arising from the HS-PEG length, contributing to further differences in the ratiometric signal between the channels. As a result, the samples will interfere with the dissociation of NPs assembly by the HS-PEGs, and a specific colorimetric signal will be obtained. Table 1 summarizes the composition of each channel

Table 1. Sensor Array Composition

Channel	1−7	8	9−15	16
PEG	HS-PEG-OMe (20, 10, 5, 2, 1, 0.75, 0.2 kDa)	HS-PEG-COOH (0.8 kDa)	HS-PEG-OMe (20, 10, 5, 2, 1, 0.75, 0.2 kDa)	HS-PEG-COOH (0.8 kDa)
NPs	AuNPs (20 nm)	AuNPs (20 nm)	AgNPs (20 nm)	AgNPs (20 nm)

of the sensor array. The sensor array consists of 16 channels (8 HS-PEGs × 2 NPs). Although the dissociative abilities of nine HS-PEGs were examined, the 350 Da HS-PEG was not utilized in the sensor array for experimental convenience (there are eight rows in a 96-well plate so only eight HS-PEGs were selected). This would also help to simplify the sensor array design by reducing the number of HS-PEGs needed, and the 0.2 kDa HS-PEG was included to account for smaller-sized HS-PEGs.

Discrimination of Microorganisms in Water. The feasibility of this sensor array design strategy was first evaluated by determining whether the sensor array could discriminate between different oral microorganism samples in water. The samples consisted of *P. gingivalis*, *F. nucleatum*, *C. albicans*, media 1 (used to culture *P.g.* and *F.n.*), and media 2 (used to culture *C.a.*) spiked in water. *P. gingivalis*, *F. nucleatum*, and *C. albicans* were selected because these microorganisms are commonly associated with oral diseases and would be present in saliva samples from patients diagnosed with periodontitis.[21,38] The working concentration of the samples was set to 10^5 cells/mL because it is representative of the limit of detection from patient samples for some biosensors.[39−42] This concentration is also representative of the physiological concentration of *P. gingivalis* found in saliva samples from patients.[43]

As a negative control, the optical response of a sample of phosphate buffer saline (PBS) solution was compared to the response of a deionized water sample. Figure 2A shows the ratiometric absorbance values for each of the conditions across the 16 channels. The mean ratiometric absorbance value for each condition was less than the mean values from the PBS and water conditions, indicating that each sample condition interfered with the effectiveness of the HS-PEG dissociation. The mean value of the PBS and water conditions was 260% greater than the mean value across all the other conditions. The number of channels was also reduced from 16 to 8 to evaluate whether the performance of the sensor array could be sustained with less sample data as shown in Figure 2B. The channels used in the simplified sensor array correspond to channels 2, 5, 6, 7, 9, 11, 14, and 16 from Table 1, and the ratiometric absorbances are tabulated in the Supporting Information (Tables S1 and S2). These channels were selected for analysis as a random subset of the 16 channels. With only 8 channels, the mean ratiometric absorbance values for the PBS and water conditions were still greater than each of other conditions, but the overall mean value was only 213% greater instead of 260%. This suggests that for these remaining 8 channels the difference in ratiometric absorbance values was not as magnified as with the 16 channels and could limit the detection of the analytes.

The ratiometric absorbances were then processed through LDA. Despite the method using a colorimetric signal, the variations in absorbance are challenging to be observed by the naked eye but can be easily discriminated using LDA. In essence, LDA seeks to project the measured responses onto two perpendicular axes that would maximize the difference in means between the groups while minimizing the variability within a group.[44,45] This is done through a matrix of coefficients (eigenvectors) of linear discriminant (LD) functions.[46] Moreover, the weighting of each LD function on the canonical score plot implies the proportion of the variance explained by that projection.[46,47] These functions allow the data to be visualized in a lower-dimensional space and identify the dimensions that best separate the groups. Each point in the plot represents a set of experimental values measured across the array of channels. The lack of overlap between the groups denotes that the conditions could be distinguished from one another.

The LDA canonical score plot indicates that the sensor array was able to discriminate between each of the sample conditions in water at the 90% confidence level. Figure 2C illustrates that the ratiometric absorbances of *P. gingivalis*, *F. nucleatum*, and *C. albicans* were not only different from one another but also differed from their corresponding culture media. This lack of overlap between the ellipses indicates that the presence of the microorganism resulted in further differences in the optical responses and suggests the effect that the microbes have on the dissociation of the NPs with the HS-PEGs. The average ratiometric absorbance value across all 16 channels was 74% greater for *P. gingivalis*, 66% greater for *F. nucleatum*, and 63% greater for *C. albicans* when compared to the average ratiometric absorbance of their corresponding culture media. Notably, the ellipses of the PBS and water samples overlapped, which confirms the need of additional analytes in the sample to produce a statistically different optical response.

Figure 2D demonstrates that the accuracy of the sensor array was mostly maintained except for one condition when the number of channels was reduced from 16 to 8 for convenience and minimizing the number of inputs required. There was an overlap in the ellipses between the *F. nucleatum* condition and its culture media condition without the additional channels. Furthermore, the proportion of the variance explained was reduced from nearly 100% with 16 channels to 94.83% with 8 channels based upon the LD1 and LD2 weightings. The detection accuracy of the sensor array was also examined using

https://doi.org/10.1021/acsami.4c15662
ACS Appl. Mater. Interfaces 2024, 16, 67362−67372

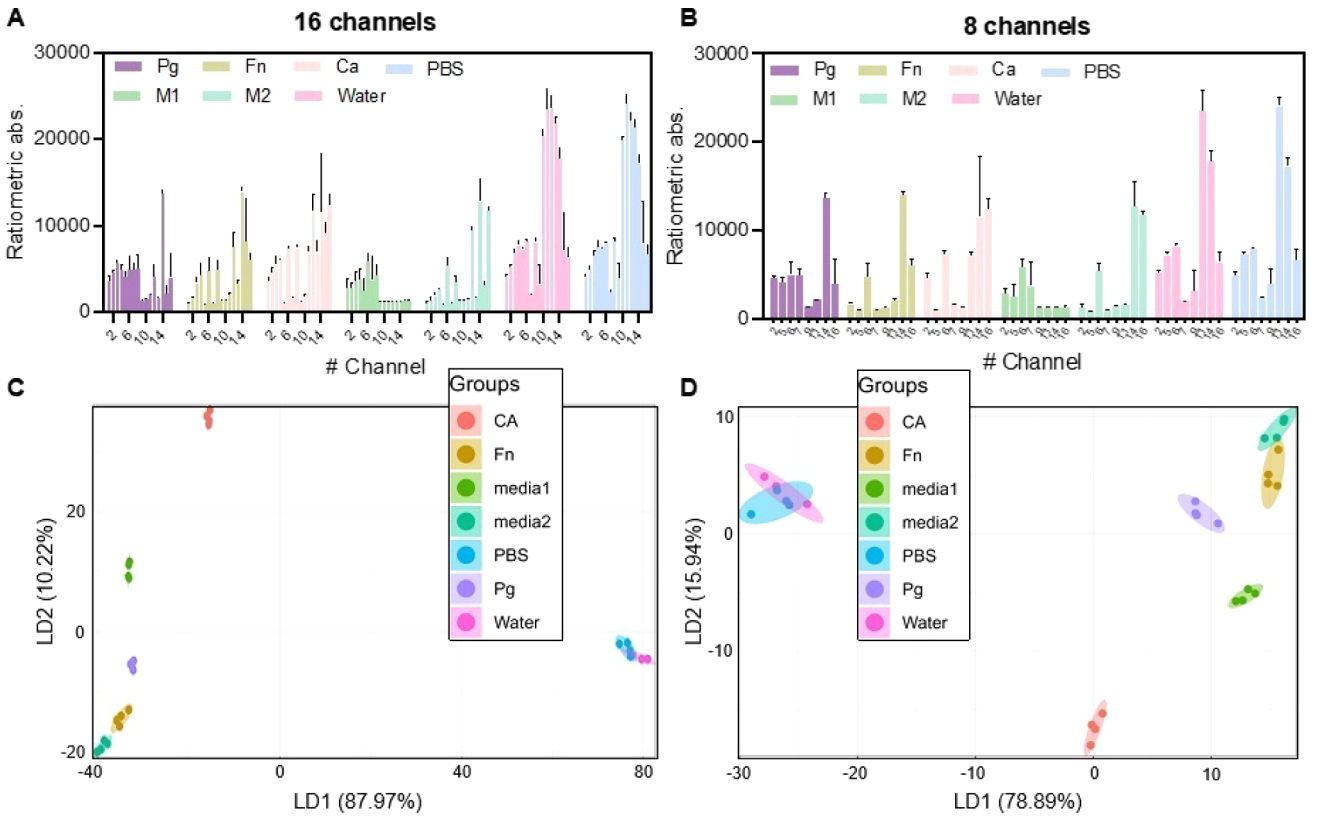

Figure 2. Discrimination of microorganisms dispersed in water (10^5 cells/mL). Panels (A) and (B) are the optical responses of deionized water samples spiked with the microorganisms in the sensor array with 16 or 8 channels respectively. The error bars represent the standard deviation from four replicates. Panels (C) and (D) are the corresponding LDA canonical score plots. They reveal that various microorganisms in water can be discriminated using this sensor array strategy and that it can be simplified by reducing the number of receptors from 16 to 8 channels. The ellipses are at the 90% confidence level.

only a single type of nanomaterial (only channels 1−8 for AuNPs and only channels 9−16 for AgNPs) as an alternative approach toward reducing the number of channels. However, the accuracy of the sensor array was also reduced by 29% with an overlap between *F. nucleatum* and the media for *C. albicans* for the AuNP subset and by 57% with several overlaps between *F. nucleatum*, *P. gingivalis*, and their corresponding media for the AgNP subset (Figures S3 and S4). This suggests that the nanoparticle type also helps to discriminate the samples in addition to the varying HS-PEG lengths used in the sensor array.

Discrimination of Microorganisms in Saliva. The sensor array design was then further evaluated by spiking the microorganisms in saliva rather than water. Figure 3A summarizes the resulting ratiometric absorbances across eight channels of the sensor array. The mean ratiometric absorbance across all the channels for *F. nucleatum* was the highest of the conditions. The average value for *F. nucleatum* was 58% greater than *C. albicans* and 22% greater than *P. gingivalis*. This indicates that *F. nucleatum* had the least hindrance in dissociating the NP assemblies compared to *P. gingivalis* and *C. albicans*. The samples were then able to be differentiated from one another through LDA as shown in Figure 3B. The proportion of explained variance was 81.85% for LD1 compared to 9.94% for LD2. This indicates that LD1 has strong discriminatory power and can effectively separate the classes in the data set in almost one dimension.

The sensor array was then tested with clinical samples of gingival cervical fluid (GCF) from patients with stage III periodontitis. The ratiometric absorbances are shown in Figure 3C, and the corresponding LDA canonical score plot is shown in Figure 3D. The values used to produce the LDA plot are tabulated in the Supporting Information (Table S3). The lack of overlap between the ellipses reveals that the sensor array was capable of discriminating samples of diseased patients from those of healthy patients at the 90% confidence level. However, the presence of other bacteria in the GCF samples likely also contribute to differences in the absorbance.

Discrimination of Viruses in Saliva. The ability to detect viruses with this sensor array design was then evaluated. Inactivated virus samples of SARS-CoV-2 and influenza were spiked in saliva at a working concentration of 10^4 RNA copies/mL, which is typical of a sample from an infected individual.[20,48] All 16 channels of the sensor array were used this time instead of only a subset of 8 because we reasoned that more channels would help to enhance the detection accuracy by providing more data to differentiate the samples. The ratiometric absorbances for the beta, delta, and omicron variants of SARS-CoV-2 and influenza viruses compared to blank saliva samples are shown in Figure 4A and summarized in the Supporting Information (Table S4). The blank saliva samples were used as a control to suggest the impact of the viruses in altering the optical response. The delta variant had the lowest average ratiometric absorbance compared to the other two variants and the influenza virus. Although the delta variant had the greatest effect in decreasing the dissociation of the NPs, the differences in the mean ratiometric absorbance values between the virus types were all within 15% of one

https://doi.org/10.1021/acsami.4c15662
ACS Appl. Mater. Interfaces 2024, 16, 67362−67372

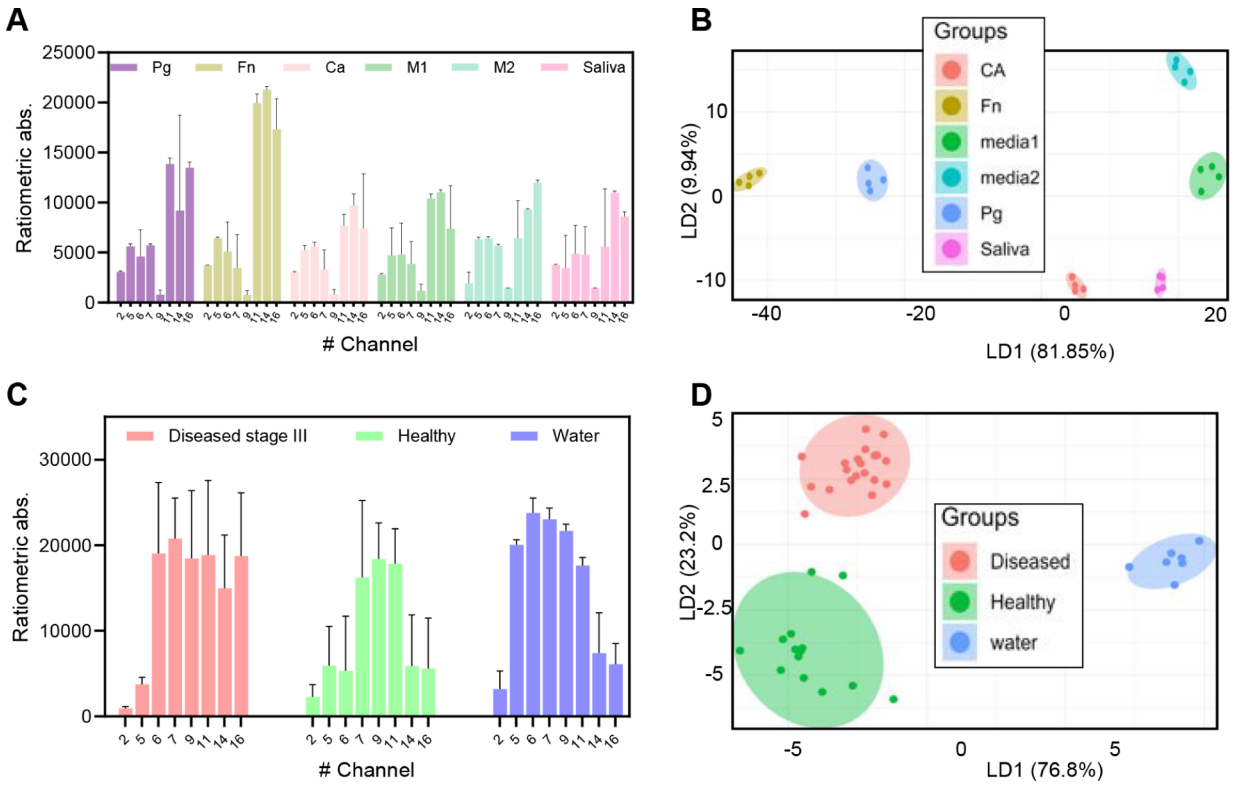

Figure 3. Discrimination of microorganisms dispersed in saliva (10^5 cells/mL). Optical responses of the sensor array for 8 channels and the associated LDA plot for discrimination of healthy saliva spiked with 10^5 cells/mL [(A) and (B)]. Panels (C) and (D) show corresponding data for saliva from patients with stage III periodontitis versus those of healthy patients. The error bars in (A) represent the standard deviation from four replicates, and the error bars in (C) represent the standard deviation from 24 samples for the diseased group, 14 samples for the healthy group, and 14 samples for the water group. The ellipses in (B) and (D) are at the 90% confidence level.

another. The discrimination of variants of SARS-CoV-2 may be due to structural differences found in the delta variant that contribute to increased interference with the peptides, the NPs, and the HS-PEGs; the spike protein of the delta variant has about 10% greater structural variation than the beta and omicron variants based on the root-mean-square deviation value of similarity with the original SARS-CoV-2 strain.[49] These mutations and conformational changes have been suggested to contribute to differences in the properties of the variants, leading to changes in their interactions and mechanism of infection with host cells.[50] However, differences in the variants might also be attributed to prep-to-prep variation in propagating, isolating, and inactivating the samples. Figure 4B shows the resulting discrimination of the samples using LDA, indicating the ability of the sensor array design to detect viruses. LD1 encapsulated 53.21% of the explained variance, while LD2 encapsulated 39.68% of the explained variance. As such, two LD functions were needed to encapsulate the variance in the conditions rather than primarily through one axis.

It was also examined whether the detection accuracy would have been maintained with a subset of the 16 channels consisting of only a single type of nanomaterial. With LDA analysis of only channels 1−8 for AuNPs and only 9−16 for AgNPs, it was found that the detection accuracy was diminished by 60% for only the AuNPs and by 40% for only the AgNPs (Figures S5 and S6). Therefore, this implies that nonspecific interactions with the nanoparticles also help to discriminate the samples rather than exclusively interactions with the different sized HS-PEGs.

Clinical saliva samples of patients diagnosed with COVID-19 were then compared to those of healthy patients with the sensor array. The saliva samples were received in collaboration with the UC San Diego Department of Medicine and were collected from COVID-19 positive patients. The optical responses from Figure 4C and the analysis with LDA at the 90% confidence level from Figure 4D indicate that the sensor array was able to discriminate healthy patients from infected patients using all 16 channels. The ratiometric absorbance values can be found in the Supporting Information (Table S5).

In comparison to other detection methods, the main advantages of this sensor array strategy are that it is simple, can operate in saliva, and can be applied to multiple analytes. While other sensing methods, such as qPCR, proteomics, and next-generation sequencing can precisely measure analyte quantity or distinguish sequence differences in organisms, these detection methods require complex analytical instruments and trained personnel that limit availability at the point-of-care.[43−46] This sensor array strategy also utilizes simple polymers to differentiate the channels in the array, while other sensor arrays require more complicated synthesis of multiple nanoparticle types with varied ligands, sizes, or shapes.[47,48] This sensor array strategy also overcomes the challenges of utilizing plasmonic nanoparticles in saliva. Other colorimetric methods may require dilution or purification to prevent the aggregation induced by the proteins and electrolytes found in biofluids.[4,49] In addition, the peptide-aggregated nanoparticles can be dried and then stored for at least one month prior to dissociation by the HS-PEGs.[19] Previous works have also shown that the aged nanoparticles have similar absorbance

https://doi.org/10.1021/acsami.4c15662
ACS Appl. Mater. Interfaces 2024, 16, 67362−67372

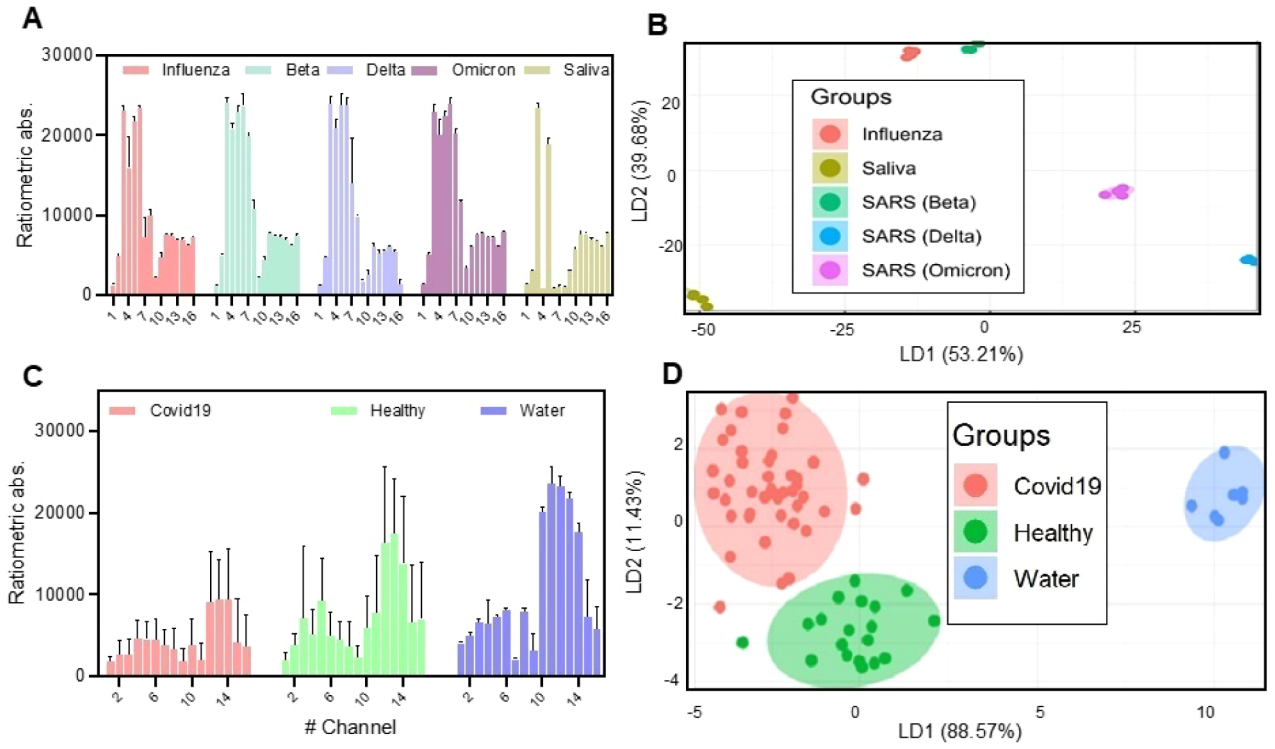

Figure 4. Discrimination of viruses dispersed in saliva (10^4 RNA copies/mL). Optical responses of the sensor array for 16 channels and the associated LDA for 10^4 RNA copies/mL inactivated viruses spiked into healthy saliva (A) and (B) or clinical saliva samples of patients diagnosed with COVID-19 versus those of healthy patients (C) and (D). The error bars in (A) represent the standard deviation from four replicates, and the error bars in (C) represent the standard deviation from 43 samples for the COVID-19 group, 19 samples for the healthy group, and 11 samples for the water group. The ellipses in (B) and (D) are at the 90% confidence level.

spectra compared to those freshly aggregated.[5] The aggregated nanoparticles can also be stored for at least 10 days without substantial changes to the absorbance spectra even at different temperature storage conditions of 4 °C, 25 °C, and 37 °C (Figure S7). The ratiometric absorbance values also were all within a 20% spread with one another (Figure S8). The increased stability of aggregated AgNPs compared to dispersed AgNPs may be because the surface of the aggregated AgNPs is coated with the RRK peptide. Therefore, the surface atoms may be protected by the peptide from redox reactions and less likely to undergo photooxidation similar to the enhanced oxidative stability of lipid coated AgNPs.[51] The sensor array can also be applied to multiple analytes without developing specific receptors for each target. In comparison, our previous work would have required engineering multiple receptors for each target analyte. In this prior work, a peptide was conjugated to the HS-PEG to quench the HS-PEG's ability to dissociate the aggregated nanoparticles.[19] The peptide contained a protease-specific cleavage sequence for *P. gingivalis* that restored the ability of the HS-PEG to dissociate the nanoparticles upon enzymatic hydrolysis. The dissociation of the nanoparticles suggested a positive signal for that particular enzyme, and, consequently, periodontal disease. In contrast, this sensor array design uses nonspecific interactions between the analyte, the nanoparticles, and the HS-PEGs to create optical patterns that can be discriminated through LDA. As such, the main advantage of this approach is that multiple analytes can be detected with this one system rather than tailoring each HS-PEG to the analyte (i.e., four different HS-PEG conjugates with peptide cleavage sequences specific to the enzymes of *P. gingivalis*, *F. nucleatum*, *C. albicans*, and SARS-CoV-2).

While promising, the current design of the sensor array requires further optimization from an end user perspective. The need for multiple sample additions for each channel of the array may prohibit adoption by users who prefer the convenience of fewer steps. Therefore, further refinement of the sensor array strategy is needed, such as with a hand-held device[50] or paper-based test strips,[51] with automated analysis before this strategy is used in commercial applications. The accuracy of the sensor array could also be improved such that the samples can be discriminated at above the 90% confidence level. Moreover, the accuracy of the sensor array could be limited by variations in the pH of the sample. At a pH of 11, the dissociative ability of the HS-PEGs was quenched (Figures S9 and S10). This may be because of deprotonation of the thiol group, which typically has a pK_a value around 10, that results in the formation of a negatively charged thiolate group.[52] Although thiolates typically have greater affinity for metallic surfaces than thiols, this negative charge would decrease the binding of the HS-PEGs with the nanoparticles due to electrostatic repulsion with the negatively charged citrate coating. Furthermore, at a pH of 3, the dissociative ability of the HS-PEG was also diminished (Figures S9 and S10). This may be the result of oxidative dissolution of the metallic surface of the nanoparticles that promotes aggregation and protonation of the citrate ligand that would reduce the electrostatic repulsion between the nanoparticles.[53,54] The protonation of the citrate ligand would facilitate aggregation by counteracting the negative charge of the citrates.[55] These factors facilitating the aggregation of the nanoparticles would

https://doi.org/10.1021/acsami.4c15662
ACS Appl. Mater. Interfaces 2024, 16, 67362−67372

make dissociation by the HS-PEGs more challenging. Therefore, the utility of this sensor array strategy may be limited at extreme pH values. However, the pH of the system is generally unlikely to reach extreme pH values. Biological samples are typically pH regulated to maintain homeostasis. For instance, saliva typically has a pH of 6.2−7.6,[56] urine typically has a pH of 4.6−8.0,[57] and plasma typically has a pH of 7.3−7.4.[58] The analyte sample also only represents approximately 10% of the final working solution volume in the sensor array so extremities in the pH of the sample would be diluted.

CONCLUSIONS

In summary, we report a simple sensor array that can operate in complex biofluid such as saliva and is cost-effective: It only uses polyethylene glycol polymers of various length as receptors and simple peptide-assembled gold or silver nanoparticles. With this sensor array, we could discriminate clinical samples of saliva either from periodontitis infected samples or COVID-19 infected samples. We hope that this sensor array design strategy will inspire and guide the development of more capable point-of-care diagnostic devices and uses for plasmonic nanoparticles. The mass production of polymers and the ability to store the peptide-assembled NPs over time will help with scaling this design strategy toward real-world applications.[19,59] Future work in developing this sensor array design includes validating functionality in other biofluids as well as advancing its versatility with other biomarkers beyond bacteria, fungi, and viruses. The incorporation of additional PEGs or other polymers of different properties (more or less hydrophilic, more or less charged, presence or absence of aromatic groups, etc.) will help to optimize the discriminatory abilities of the sensor array and allow for reductions in the number of channels required. The limit of detection of the sensor array should also be determined once the sensor array design has been further refined.

ASSOCIATED CONTENT

Supporting Information

The Supporting Information is available free of charge at https://pubs.acs.org/doi/10.1021/acsami.4c15662.

Materials, TEM of the NPs, linear regression analysis of the HS-PEG size, LDA of a subset of the sensor array channels, evaluation of nanoparticle stability and pH effects, matrices for LDA (PDF)

AUTHOR INFORMATION

Corresponding Authors

Maurice Retout − *Aiiso Yufeng Li Family Department of Chemical and Nano Engineering, University of California, San Diego, La Jolla, California 92093, United States;* orcid.org/0000-0002-8140-6621; Email: Maurice.retout@ulb.be

Jesse V. Jokerst − *Aiiso Yufeng Li Family Department of Chemical and Nano Engineering, Materials Science and Engineering Program, and Department of Radiology, University of California, San Diego, La Jolla, California 92093, United States;* orcid.org/0000-0003-2829-6408; Email: jjokerst@ucsd.edu

Authors

Benjamin Lam − *Aiiso Yufeng Li Family Department of Chemical and Nano Engineering, University of California, San Diego, La Jolla, California 92093, United States;* orcid.org/0009-0004-3616-1583

Lubna Amer − *Materials Science and Engineering Program, University of California, San Diego, La Jolla, California 92093, United States;* orcid.org/0000-0001-5715-5060

Elizabeth Thompson − *Department of Chemistry, Truman State University, Kirksville, Missouri 63501, United States*

Alex E. Clark − *Department of Medicine, University of California, San Diego, La Jolla, California 92093, United States*

Aaron F. Garretson − *Department of Medicine, University of California, San Diego, La Jolla, California 92093, United States*

Aaron F. Carlin − *Department of Medicine and Department of Pathology, University of California, San Diego, La Jolla, California 92093, United States;* orcid.org/0000-0002-1669-8066

Casey Chen − *Herman Ostrow School of Dentistry, University of Southern California, Los Angeles, California 90089, United States*

Complete contact information is available at: https://pubs.acs.org/10.1021/acsami.4c15662

Notes

The authors declare no competing financial interest.

ACKNOWLEDGMENTS

J.V.J. acknowledges funding from NIH under grants R01 DE031114, R21 AG0657776-01S1, and R21 AI157957. J.V.J. also acknowledges the generous support of The Shiley Foundation. A.F.C. is supported by a Career Award for Medical Scientists from the Burroughs Wellcome Fund. We also acknowledge infrastructure support under NIH S10 OD023555. The authors acknowledge the use of facilities and instrumentation supported by NSF through the UC San Diego Materials Research Science and Engineering Center (UCSD MRSEC), grant # DMR-2011924. The authors thank the University of California, San Diego - Cellular and Molecular Medicine Electron Microscopy Core (UCSD-CMM-EM Core, RRID: SCR_022039) for equipment access and technical assistance (partly supported by NIH award S10 OD023527). Figures were made using icons from BioRender.com.

REFERENCES

(1) Zhao, V. X. T.; Wong, T. I.; Zheng, X. T.; Tan, Y. N.; Zhou, X. Colorimetric biosensors for point-of-care virus detections. *Mater. Sci. Energy Technol.* **2020**, *3*, 237−249.

(2) Heifler, O.; Borberg, E.; Harpak, N.; Zverzhinetsky, M.; Krivitsky, V.; Gabriel, I.; Fourman, V.; Sherman, D.; Patolsky, F. Clinic-on-a-Needle Array toward Future Minimally Invasive Wearable Artificial Pancreas Applications. *ACS Nano* **2021**, *15* (7), 12019−12033.

(3) Kim, E. R.; Joe, C.; Mitchell, R. J.; Gu, M. B. Biosensors for healthcare: current and future perspectives. *Trends Biotechnol.* **2023**, *41* (3), 374−395.

(4) Alberti, G.; Zanoni, C.; Magnaghi, L. R.; Biesuz, R. Gold and Silver Nanoparticle-Based Colorimetric Sensors: New Trends and Applications. *Chemosensors* **2021**, *9* (11), 305.

(5) Retout, M.; Jin, Z.; Tsujimoto, J.; Mantri, Y.; Borum, R.; Creyer, M. N.; Yim, W.; He, T.; Chang, Y.-C.; Jokerst, J. V. Di-Arginine Additives for Dissociation of Gold Nanoparticle Aggregates: A Matrix-Insensitive Approach with Applications in Protease Detection. *ACS Appl. Mater. Interfaces* **2022**, *14* (46), 52553−52565.

(6) Moros, M.; Kyriazi, M.-E.; El-Sagheer, A. H.; Brown, T.; Tortiglione, C.; Kanaras, A. G. DNA-Coated Gold Nanoparticles for the Detection of mRNA in Live Hydra Vulgaris Animals. *ACS Appl. Mater. Interfaces* **2019**, *11* (15), 13905−13911.
(7) Nietzold, C.; Lisdat, F. Fast protein detection using absorption properties of gold nanoparticles. *Analyst* **2012**, *137* (12), 2821−2826.
(8) Kim, Y.; Johnson, R. C.; Hupp, J. T. Gold Nanoparticle-Based Sensing of "Spectroscopically Silent" Heavy Metal Ions. *Nano Lett.* **2001**, *1* (4), 165−167.
(9) Jin, Z.; Mantri, Y.; Retout, M.; Cheng, Y.; Zhou, J.; Jorns, A.; Fajtova, P.; Yim, W.; Moore, C.; Xu, M.; Creyer, M. N.; Borum, R. M.; Zhou, J.; Wu, Z.; He, T.; Penny, W. F.; O'Donoghue, A. J.; Jokerst, J. V. A Charge-Switchable Zwitterionic Peptide for Rapid Detection of SARS-CoV-2 Main Protease. *Angew. Chem., Int. Ed.* **2022**, *61* (9), No. e202112995.
(10) Hu, T.; Lu, S.; Chen, C.; Sun, J.; Yang, X. Colorimetric sandwich immunosensor for Aβ(1−42) based on dual antibody-modified gold nanoparticles. *Sens. Actuators, B* **2017**, *243*, 792−799.
(11) Lin, J.-H.; Huang, K.-H.; Zhan, S.-W.; Yu, C.-J.; Tseng, W.-L.; Hsieh, M.-M. Inhibition of catalytic activity of fibrinogen-stabilized gold nanoparticles via thrombin-induced inclusion of nanoparticle into fibrin: Application for thrombin sensing with more than 104-fold selectivity. *Spectrochim. Acta, Part A* **2019**, *210*, 59−65.
(12) Peng, H.; Borg, R. E.; Nguyen, A. B. N.; Chen, I. A. Chimeric Phage Nanoparticles for Rapid Characterization of Bacterial Pathogens: Detection in Complex Biological Samples and Determination of Antibiotic Sensitivity. *ACS Sens.* **2020**, *5* (5), 1491−1499.
(13) Bigdeli, A.; Ghasemi, F.; Golmohammadi, H.; Abbasi-Moayed, S.; Nejad, M. A. F.; Fahimi-Kashani, N.; Jafarinejad, S.; Shahrajabian, M.; Hormozi-Nezhad, M. R. Nanoparticle-based optical sensor arrays. *Nanoscale* **2017**, *9* (43), 16546−16563.
(14) Peveler, W. J. Food for Thought: Optical Sensor Arrays and Machine Learning for the Food and Beverage Industry. *ACS Sens.* **2024**, *9* (4), 1656−1665.
(15) Boselli, L.; Castagnola, V.; Armirotti, A.; Benfenati, F.; Pompa, P. P. Biomolecular Corona of Gold Nanoparticles: The Urgent Need for Strong Roots to Grow Strong Branches. *Small* **2024**, *20* (15), 2306474.
(16) Wang, J.; Drelich, A. J.; Hopkins, C. M.; Mecozzi, S.; Li, L.; Kwon, G.; Hong, S. Gold nanoparticles in virus detection: Recent advances and potential considerations for SARS-CoV-2 testing development. *Wiley Interdiscip. Rev.: Nanomed. Nanobiotechnol.* **2022**, *14* (1), No. e1754.
(17) Pino, P. D.; Pelaz, B.; Zhang, Q.; Maffre, P.; Nienhaus, G. U.; Parak, W. J. Protein corona formation around nanoparticles − from the past to the future. *Mater. Horiz.* **2014**, *1* (3), 301−313.
(18) Rampado, R.; Crotti, S.; Caliceti, P.; Pucciarelli, S.; Agostini, M. Recent Advances in Understanding the Protein Corona of Nanoparticles and in the Formulation of "Stealthy" Nanomaterials. *Front. Bioeng. Biotechnol.* **2020**, *8*, 166.
(19) Retout, M.; Amer, L.; Yim, W.; Creyer, M. N.; Lam, B.; Trujillo, D. F.; Potempa, J.; O'Donoghue, A. J.; Chen, C.; Jokerst, J. V. A Protease-Responsive Polymer/Peptide Conjugate and Reversible Assembly of Silver Clusters for the Detection of Porphyromonas gingivalis Enzymatic Activity. *ACS Nano* **2023**, *17* (17), 17308−17319.
(20) Lam, B.; Retout, M.; Clark, A. E.; Garretson, A. F.; Carlin, A. F.; Jokerst, J. V. Silver Nanoparticle Sensor Array for the Detection of SARS-CoV-2. *ACS Appl. Nano Mater.* **2024**, *7* (8), 9136−9146.
(21) Amer, L.; Retout, M.; Jokerst, J. V. Activatable prodrug for controlled release of an antimicrobial peptide via the proteases overexpressed in Candida albicans and Porphyromonas gingivalis. *Theranostics* **2024**, *14* (4), 1781−1793.
(22) Ha, S.; Kim, K. T. Effect of hydrophilic block end groups and block junction on block copolymer self-assembly in solution. *RSC Adv.* **2022**, *12* (12), 7446−7452.
(23) Benhabbour, S. R.; Sheardown, H.; Adronov, A. Protein Resistance of PEG-Functionalized Dendronized Surfaces: Effect of PEG Molecular Weight and Dendron Generation. *Macromolecules* **2008**, *41* (13), 4817−4823.
(24) Cho, B.; Charoensri, K.; Doh, H.; Park, H. J. Preparation of Colorimetric Sensor Array System to Evaluate the Effects of Alginate Edible Coating on Boiled-Dried Anchovy. *Foods* **2023**, *12*, 638.
(25) Wei, H.; Hossein Abtahi, S. M.; Vikesland, P. J. Plasmonic colorimetric and SERS sensors for environmental analysis. *Environ. Sci.: Nano* **2015**, *2* (2), 120−135.
(26) Subara, D.; Jaswir, I. Gold Nanoparticles: Synthesis and application for Halal Authentication in Meat and Meat Products. *Int. J. Adv. Sci., Eng. And Inform. Technol.* **2018**, *8* (4−2), 1633−1641.
(27) Aftenieva, O.; Schletz, D.; Offenhäußer, T.; Riesterer, J.; Schmalzriedt, S.; König, T. A. F. Expanding the Plasmonic Color Palette: Enhancing Nanotechnology Education through a User-Friendly Teaching Platform. *J. Chem. Educ.* **2024**, *101* (8), 3311−3317.
(28) Bélteky, P.; Rónavári, A.; Zakupszky, D.; Boka, E.; Igaz, N.; Szerencsés, B.; Pfeiffer, I.; Vágvölgyi, C.; Kiricsi, M.; Kónya, Z. Are Smaller Nanoparticles Always Better? Understanding the Biological Effect of Size-Dependent Silver Nanoparticle Aggregation Under Biorelevant Conditions. *Int. J. Nanomed.* **2021**, *16*, 3021−3040.
(29) Pozzi, M.; Jonak Dutta, S.; Kuntze, M.; Bading, J.; Rüßbült, J. S.; Fabig, C.; Langfeldt, M.; Schulz, F.; Horcajada, P.; Parak, W. J. Visualization of the High Surface-to-Volume Ratio of Nanomaterials and Its Consequences. *J. Chem. Educ.* **2024**, *101* (8), 3146−3155.
(30) Kawai, S.; Foster, A. S.; Björkman, T.; Nowakowska, S.; Björk, J.; Canova, F. F.; Gade, L. H.; Jung, T. A.; Meyer, E. Van der Waals interactions and the limits of isolated atom models at interfaces. *Nat. Commun.* **2016**, *7* (1), 11559.
(31) Luo, Y.; Zhao, R.; Pendry, J. B. van der Waals interactions at the nanoscale: The effects of nonlocality. *Proc. Natl. Acad. Sci. U.S.A.* **2014**, *111* (52), 18422−18427.
(32) Adewale, O. B.; Davids, H.; Cairncross, L.; Roux, S. Toxicological Behavior of Gold Nanoparticles on Various Models: Influence of Physicochemical Properties and Other Factors. *Int.J. Toxicol.* **2019**, *38* (5), 357−384.
(33) Yim, W.; Retout, M.; Chen, A. A.; Ling, C.; Amer, L.; Jin, Z.; Chang, Y.-C.; Chavez, S.; Barrios, K.; Lam, B.; Li, Z.; Zhou, J.; Shi, L.; Pascal, T. A.; Jokerst, J. V. Correction to "Goldilocks Energy Minimum: Peptide-Based Reversible Aggregation and Biosensing. *ACS Appl. Mater. Interfaces* **2023**, *15* (41), 48838−48838.
(34) Schneider, C. P.; Shukla, D.; Trout, B. L. Arginine and the Hofmeister Series: The Role of Ion−Ion Interactions in Protein Aggregation Suppression. *J. Phys. Chem. B* **2011**, *115* (22), 7447−7458.
(35) Sun, Y.; Xia, Y. Gold and silver nanoparticles: A class of chromophores with colors tunable in the range from 400 to 750 nm. *Analyst* **2003**, *128* (6), 686−691.
(36) Jokerst, J. V.; Lobovkina, T.; Zare, R. N.; Gambhir, S. S. Nanoparticle PEGylation for Imaging and Therapy. *Nanomedicine* **2011**, *6* (4), 715−728.
(37) Jin, Z.; Yim, W.; Retout, M.; Housel, E.; Zhong, W.; Zhou, J.; Strano, M. S.; Jokerst, J. V. Colorimetric sensing for translational applications: From colorants to mechanisms. *Chem. Soc. Rev.* **2024**, *53*, 7681.
(38) Delaney, C.; Kean, R.; Short, B.; Tumelty, M.; McLean, W.; Nile, C. J.; Ramage, G. Fungi at the Scene of the Crime: Innocent Bystanders or Accomplices in Oral Infections? *Curr. Clin. Microbiol. Rep.* **2018**, *5* (3), 190−200.
(39) Pan, C.; Liu, J.; Wang, H.; Song, J.; Tan, L.; Zhao, H. Porphyromonas gingivalis can invade periodontal ligament stem cells. *BMC Microbiol.* **2017**, *17* (1), 38.
(40) O'Brien-Simpson, N. M.; Burgess, K.; Brammar, G. C.; Darby, I. B.; Reynolds, E. C. Development and evaluation of a saliva-based chair-side diagnostic for the detection of Porphyromonas gingivalis. *J. Oral Microbiol.* **2015**, *7* (1), 29129.
(41) Hussain, K. K.; Malavia, D.; Johnson, E. M.; Littlechild, J.; Winlove, C. P.; Vollmer, F.; Gow, N. A. R. Biosensors and Diagnostics for Fungal Detection. *J. Fungi.* **2020**, *6* (4), 349.

https://doi.org/10.1021/acsami.4c15662
ACS Appl. Mater. Interfaces 2024, 16, 67362−67372

(42) Guliy, O. I.; Karavaeva, O. A.; Smirnov, A. V.; Eremin, S. A.; Bunin, V. D. Optical Sensors for Bacterial Detection. *Sensors* **2023**, *23* (23), 9391.
(43) O'Brien-Simpson, N. M.; Burgess, K.; Lenzo, J. C.; Brammar, G. C.; Darby, I. B.; Reynolds, E. C. Rapid Chair-Side Test for Detection of Porphyromonas gingivalis. *J. Dent. Res.* **2017**, *96* (6), 618−625.
(44) Boedeker, P.; Kearns, N. T. Linear Discriminant Analysis for Prediction of Group Membership: A User-Friendly Primer. *Adv. Methods Pract. Psychol. Sci.* **2019**, *2* (3), 250−263.
(45) Gardner-Lubbe, S. Linear discriminant analysis for multiple functional data analysis. *J. Appl. Stat.* **2021**, *48* (11), 1917−1933.
(46) Bakker, J. D. *Applied Multivariate Statistics in R*; University of Washington, 2024. https://uw.pressbooks.pub/appliedmultivariatestatistics/.
(47) Dhamnetiya, D.; Goel, M. K.; Jha, R. P.; Shalini, S.; Bhattacharyya, K. How to Perform Discriminant Analysis in Medical Research? Explained with Illustrations. *J. Lab. Phys.* **2022**, *14* (4), 511−520.
(48) Jenney, A.; Chibo, D.; Batty, M.; Druce, J.; Melvin, R.; Stewardson, A.; Dennison, A.; Symes, S.; Kinsella, P.; Tran, T.; et al. Surveillance testing using salivary RT-PCR for SARS-CoV-2 in managed quarantine facilities in Australia: A laboratory validation and implementation study. *Lancet Regional Health − Western Pacific* **2022**, *26*, 100533.
(49) Alam, M. M.; Hannan, S. B.; Saikat, T. A.; Limon, M. B. H.; Topu, M. R.; Rana, M. J.; Salauddin, A.; Bosu, S.; Rahman, M. Z. Beta, Delta, and Omicron, Deadliest Among SARS-CoV-2 Variants: A Computational Repurposing Approach. *Evol. Bioinform. Online* **2023**, *19*, 11769343231182258.
(50) Du, X.; Tang, H.; Gao, L.; Wu, Z.; Meng, F.; Yan, R.; Qiao, S.; An, J.; Wang, C.; Qin, F. X.-F. Omicron adopts a different strategy from Delta and other variants to adapt to host. *Signal Transduction Targeted Ther.* **2022**, *7* (1), 45.
(51) Cunningham, B.; Engstrom, A. M.; Harper, B. J.; Harper, S. L.; Mackiewicz, M. R. Silver Nanoparticles Stable to Oxidation and Silver Ion Release Show Size-Dependent Toxicity In Vivo. *Nanomaterials* **2021**, *11* (6), 1516.
(52) Thapa, B.; Schlegel, H. B. Density Functional Theory Calculation of pKa's of Thiols in Aqueous Solution Using Explicit Water Molecules and the Polarizable Continuum Model. *J. Phys. Chem. A* **2016**, *120* (28), 5726−5735.
(53) Fernando, I.; Zhou, Y. Impact of pH on the stability, dissolution and aggregation kinetics of silver nanoparticles. *Chemosphere* **2019**, *216*, 297−305.
(54) Adamczyk, Z.; Oćwieja, M.; Mrowiec, H.; Walas, S.; Lupa, D. Oxidative dissolution of silver nanoparticles: A new theoretical approach. *J. Colloid Interface Sci.* **2016**, *469*, 355−364.
(55) Lambros, M.; Tran, T. H.; Fei, Q.; Nicolaou, M. Citric Acid: A Multifunctional Pharmaceutical Excipient. *Pharmaceutics* **2022**, *14* (5), 972.
(56) Baliga, S.; Muglikar, S.; Kale, R. Salivary pH: A diagnostic biomarker. *J. Indian Soc. Periodontol.* **2013**, *17* (4), 461−465.
(57) Yıldırım, I.; Koçan, H. The pH of Drinking Water and Its Effect on the pH of Urine. *Cureus* **2023**, *15* (10), No. e47437.
(58) Atherton, J. C. Acid−base balance: maintenance of plasma pH. *Anaesth. Int. Care Med.* **2009**, *10* (11), 557−561.
(59) Li, J.; Kao, W. J. Synthesis of Polyethylene Glycol (PEG) Derivatives and PEGylated−Peptide Biopolymer Conjugates. *Biomacromolecules* **2003**, *4* (4), 1055−1067.

https://doi.org/10.1021/acsami.4c15662
ACS Appl. Mater. Interfaces 2024, 16, 67362−67372